Interseismic coupling, segmentation and mechanical behavior of the Central Chile subduction zone.

M. Métois, Anne Socquet, C. Vigny

Interseismic coupling, segmentation and mechanical behavior of the central Chile subduction zone

M. Métois,[1,2] A. Socquet,[2,3] and C. Vigny[1]

Received 2 August 2011; revised 7 January 2012; accepted 17 January 2012; published 14 March 2012.

[1] Global Positioning System (GPS) measurements carried out in Chile over the last two decades showed that an entire portion of the Nazca-South America subduction zone (38°S − 24°S) was locked over this period of time. The induced accumulation of elastic deformation in the upper-plate was not released until the recent Maule earthquake of 27 February 2010 (M_w 8.8) that ruptured the southern part of this section. Locking or coupling between the two plates varies both with depth and along strike. Here we use our own GPS data (an updated solution of our extended network in central Chile), combined with other published data sets, to quantify the spatial variations of the coupling that prevailed before the Maule earthquake. Using a simple elastic model based on the back-slip assumption, we show that coupling variations on the subduction plane are sufficient to explain the observed surface deformation, with no need of a sliver in central Chile. We identify four segments characterized by higher coupling and separated by narrow areas of lower coupling. This segmentation is in good agreement with historical and recent seismicity in Chile. In particular the narrow zones of lower coupling seem to have stopped most large seismic ruptures, including Maule's. These zones are often associated with irregular bathymetric or coastal features (fracture zones or peninsulas). Finally, coseismic and early post-seismic slip distribution of the Maule earthquake, occurring either in previously highly or weakly coupled zones, map a complex distribution of velocity-weakening and velocity-strengthening patches on the subduction interface.

Citation: Métois, M., A. Socquet, and C. Vigny (2012), Interseismic coupling, segmentation and mechanical behavior of the central Chile subduction zone, *J. Geophys. Res.*, *117*, B03406, doi:10.1029/2011JB008736.

1. Introduction

[2] Many major earthquakes have occurred along the Chile subduction zone, where the Nazca and the South-America plates converge at rates among the highest on Earth (68 mm/yr [e.g., *Altamimi et al.*, 2007]). The most significant events are the M_w 9.5 1960 Valdivia earthquake [*Plafker and Savage*, 1970; *Cifuentes*, 1989; *Campos et al.*, 2002] and the more recent M_w 8.8 February 2010 Maule event [e.g., *Delouis et al.*, 2010; *Vigny et al.*, 2011] (Figure 1). Between two successive earthquakes at the same location, i.e., during the "interseismic phase" of the seismic cycle, full or partial coupling on the subduction interface accumulates elastic strain energy in both plates, which can be released during the coseismic phase. Here coupling is defined as the ratio between interseismic slip rate of the subduction interface and the plates convergence velocity.

[3] Models dividing subduction interface into four along-dip zones have been proposed [*Hyndman et al.*, 1997; *Oleskevich et al.*, 1999]. First, in these models, an updip zone near the trench is characterized by a velocity-strengthening behavior controlled by the presence of fluid-rich sediments at the interface. Recent studies showed that megathrust rupture can propagate updip through this area [*Lay et al.*, 2010; *Vigny et al.*, 2011; *Ide et al.*, 2011]. Second, the "locked" or "seismogenic" zone is composed of seismic asperities that rupture during the coseismic phase with a velocity-weakening behavior [*Ruff and Kanamori*, 1983]. Third, the downdip zone is seen as an intermediate area between the locked zone and the deep creep zone, although its mechanical behavior is still poorly understood. Last, the deepest part of the interface steadily creeps at the plate convergence rate.

[4] Validating this zonation model requires more observational constraints. In particular, dense geodetic measurements are needed to image the along-trench and along-dip variability of the interseismic coupling. Together with seismological and structural data, accurate maps of the interseismic coupling should improve our understanding of the connection between the segmentation of the megathrust and its behavior during the whole seismic cycle. Furthermore, assessing the interseismic coupling in zones identified as "seismic gaps" should clarify whether those gaps are

[1]Laboratoire de Géologie, UMR 8538, Ecole Normale Supérieure, Paris, France.
[2]Équipe de Tectonique, Institut de Physique du Globe de Paris, Sorbonne Paris Cité, Université Paris Diderot, UMR 7154 CNRS, Paris, France.
[3]Now at Institut des Sciences de la Terre, Université de Grenoble 1, CNRS, Grenoble, France.

0148-0227/12/2011JB008736

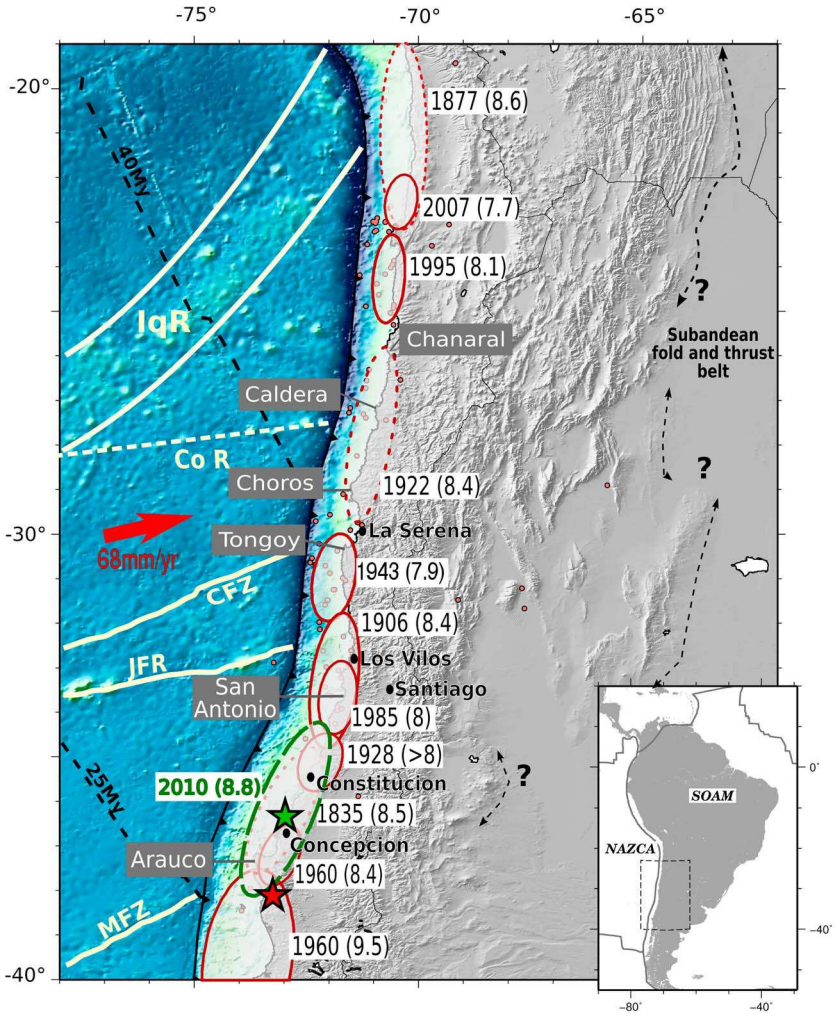

Figure 1. Seismotectonic background of the NAZCA-SOAM convergence zone and main geological features. Topography and bathymetry are from ETOPO1. The possible fronts of the sub-Andean fold and thrust belt are marked with black dashed lines. White lines: contours of bathymetric features of the Nazca subducting plate. IqR: Iquique ridge, Co R: Copiapo Ridge, CFZ: Challenger fracture zone, JFR: Juan Fernandez ridge, MFZ: Mocha Fracture Zone. Black dashed lines: isochrons of Nazca plate ocean floor extracted from [*Muller et al.*, 1997]. The bold red arrow represents the convergence of NAZCA plate with respect to SOAM plate. Red contoured ellipses: maximal rupture zones of the M>7.5 historical (dashed) and instrumental (solid) earthquakes since 1830 (from Servicio Sismologico Nacional catalog (http://ssn.dgf.uchile.cl/) [*Beck et al.*, 1998; *Comte and Pardo*, 1991; *Biggs and Robinson*, 2009] see also http://earthquake.usgs.gov/research/data/centennial.php). Green ellipse: rupture zone of the 2010 Maule earthquake. Green star: relocated hypocenter for the Maule event [*Vigny et al.*, 2011]. Red circles: M_w>6 events since 1976 (http://www.globalcmt.org/CMTsearch.html). Peninsulas and coastal features are named on the grey rectangles.

permanent aseismic creeping areas where seismic hazard is low, or fully locked zones where seismic hazard is high.

[5] The Chilean subduction zone is an ideal natural laboratory to quantify the spatial variations of interseismic coupling, because of its fast convergence rates, its relatively simple structure (e.g. no slip partitioning in its central part [*Hoffmann-Rothe et al.*, 2006]), and dense GPS monitoring since the 1990s. To study these spatial variations, we use a kinematic approach in which we invert all available GPS data depicting interseismic deformation in central Chile (between 38°Sand 24°S) [*Klotz et al.*, 2001; *Khazaradze and Klotz*, 2003; *Brooks et al.*, 2003; *Ruegg et al.*, 2009; *Vigny et al.*, 2009]. In north-central Chile, we use an updated solution from *Vigny et al.* [2009] that includes additional measurements in 2007 and 2008 on an otherwise extended network (see Text S1 of the auxiliary material).[1] This study allows us (1) to inspect the correlation between interseismic coupling and seismic ruptures along the Chilean subduction zone, (2) to assess the coupling distribution on the

[1]Auxiliary materials are available in the HTML. doi:10.1029/2011JB008736.

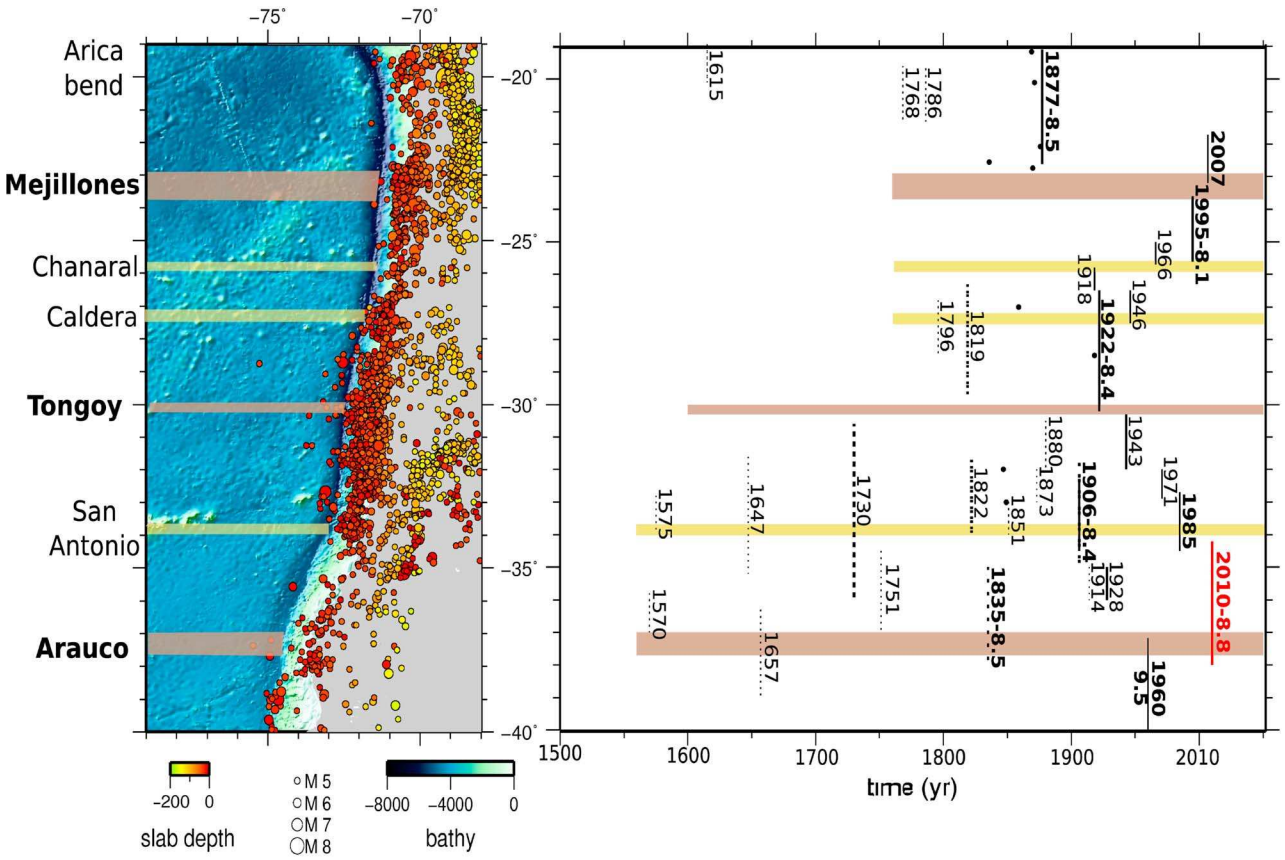

Figure 2. Historical and instrumental seismicity along the Chilean trench. (left) Dots depict the seismicity (M_w>5) recorded since 1990 (CMT catalog). Magnitude and depth (in km) of the epicenters are coded by the dot's size and color, respectively. (right) Largest estimated rupture lengths of the main identified historical earthquakes since 1500 against time. Dashed and solid lines mean high and low uncertainty on those ruptures, respectively [*Lomnitz*, 1970; *Beck et al.*, 1998; *Campos et al.*, 2002] (see also http://earthquake.usgs.gov/research/data/centennial.php). M_w is indicated for well studied major events. Red solid line: recent 2010 Maule rupture zone. Black circles: epicenters of less important and documented events. Brown and yellow horizontal strips underline the seismic segmentation. Brown lines are intersegment barriers that are rarely crossed by the seismic ruptures, whereas yellow ones are less persistent barriers.

former Maule seismic gap, (3) to investigate which physical parameters control interseismic coupling, and (4) to identify zones that experience both aseismic and coseismic slip. We show that the interseismic coupling is segmented along the Chilean subduction zone. We discuss the relationship between those coupling variations and other segmentation markers, namely, the occurrence of structural complexities along the Chilean coast, the subduction of bathymetric features on the subducting plate, the distribution of previous large earthquakes, and lateral variations in the seismicity rate. We propose a first-order mechanical interpretation of the kinematic coupling and its potential role in promoting or stopping seismic propagation. In particular we perform a detailed comparison of interseismic loading versus co- and post- seismic moment release in the Maule segment.

2. Seismotectonic Context

[6] The Nazca and South American plates converge with an average velocity of 68 mm/yr [e.g., *Altamimi et al.*, 2007]. The convergence is oblique, but in central Chile this obliquity does not generate slip partitioning, which is the opposite of what is observed in Sumatra [*Fitch*, 1972]. South of the Arauco peninsula (38°S), partitioning exists where the Liquiñe-Ofqui strike-slip fault system accommodates a resolvable motion (more than 4 mm/yr) [*Moreno et al.*, 2008; *Melnick and Bookhagen*, 2009]. In the Altiplano area (north of 24°S), the active Argentine sub-Andean fold and thrust belt may accommodate part of the convergence (up to 10 mm/yr [*Norabuena et al.*, 1998; *Bevis et al.*, 2001], see Figure 1).

[7] The historical seismicity of the Chilean subduction zone has been unevenly recorded since the 16th century, but much more evenly and hence more reliably since the 1850's [*Lomnitz*, 1970]. The analysis of these records outlines a segmentation based on the recurrence of subduction earthquakes that repeatedly rupture roughly the same areas (see Figures 1 and 2) [*Lomnitz*, 1970; *Comte and Pardo*, 1991; *Beck et al.*, 1998; *Biggs and Robinson*, 2009]. For example,

the North Chile segment (19°S to ~ 24°S [*Nishenko*, 1991]) or the Maule segment (38°S to 34°S [*Campos et al.*, 2002]) were identified as seismic gaps that had not experienced a large megathrust earthquake since 1877 and 1835, respectively. In addition, these two segments have experienced less intermediate-magnitude seismicity on the subduction interface since 1976 (the start of the U.S. Geological Survey USGS catalog) than the adjacent segments [*Campos et al.*, 2002] (Figure 2). The segment at the latitude range of the Metropolitan area (34°S to 30°S) was most probably fully ruptured by the M_w 8.4 Valparaiso earthquake in 1906, and then partially broken in 1943, 1971 and 1985. Further north, from 30°S to 25°S, the last major subduction earthquake occurred in 1922.

[8] Singular coastal features, such as bays and peninsulas associated with dense crustal fault networks, often correlate with the termination or nucleation of major ruptures (see Figures 1 and 2) [*Armijo and Thiele*, 1990; *Moreno et al.*, 2008; *Audin et al.*, 2008; *Melnick and Bookhagen*, 2009]. For example, in northern Chile, the Mejillones peninsula coincided with the end of the 2007 Tocopilla rupture [*Béjar-Pizarro et al.*, 2009; *Peyrat et al.*, 2010] and is just north of the start of the 1995 Antofagasta event [*Ruegg et al.*, 1996; *Chlieh et al.*, 2004; *Pritchard and Simons*, 2006]. Another example is the Arauco peninsula where the 1960 Valdivia main rupture started [*Plafker and Savage*, 1970; *Cifuentes*, 1989; *Campos et al.*, 2002]. Many of those peninsulas correlate with the subduction of irregular bathymetric features of the downgoing oceanic plate (ridges and fracture zones): the Mocha Fracture Zone (MFZ) subducts just south of the Arauco peninsula (38°S); the Challenger fracture zone (CFZ) -which separates two seafloor sections of different ages [*Muller et al.*, 1997] (Figure 1)- subducts in front of the Tongoy peninsula (30°S); the Nazca ridge subducts south of the Pisco peninsula (15°S) and the large Iquique Ridge (IqR) subducts in the North Chile gap (from 18 to 21 °S) (Figure 1).

[9] This apparent correlation between morphologic features of the involved plates and the rupture zones of past earthquakes outlines a possible seismotectonic segmentation of the Chilean trench. However, no single physical parameter commonly invoked as controlling factor of subduction behavior (e.g. rheology and crustal faulting of the upper plate, depth of the continental Moho, bathymetry, age and density of the subducting plate, sediment or fluids amount, thermal variations) is sufficient to explain this segmentation pattern. This implies that the physical nature of the segments, their boundaries, interaction and behavior remain poorly understood.

3. GPS Data Compilation

[10] Previous studies have attempted to quantify coupling on the subduction interface, as constrained from the surface deformation measured by GPS. *Klotz et al.* [2001] and *Khazaradze and Klotz* [2003] assume 100% uniform locking and invert for depth variations of the locked zone only. *Bevis et al.* [2001] and *Brooks et al.* [2003] use a 100% locked interface, fix the downdip extent of this locked zone and invert for the motion of an Andean sliver included in a 3-plate model. These previous studies, which use very large-scale networks with distances of ~100 km or more between GPS sites, lack the resolution necessary to resolve heterogeneous coupling on the subduction interface. These models show large residuals at many coastal sites (more than 10 mm/yr at some sites for *Klotz et al.* [2001] and more than 5 mm/yr for *Bevis et al.* [2001]). This reveals short-scale lateral variations of the coupling coefficient that were yet underlined by previous local studies [*Ruegg et al.*, 2009; *Vigny et al.*, 2009].

[11] Here, we combine published French-Chilean measurements (LiA, International Associated Laboratory) in southern Chile [*Ruegg et al.*, 2009] with those of the SAGA [*Klotz et al.*, 2001; *Khazaradze and Klotz*, 2003; *Moreno et al.*, 2008] and CAP [*Bevis et al.*, 2001; *Kendrick et al.*, 2001; *Brooks et al.*, 2003] teams. We add to those data sets an extended and improved version of the French-Chilean central network data set originally published by *Vigny et al.* [2009] (see Text S1 of the auxiliary material). We thus gather 263 horizontal GPS velocities into a single data set. Because the older data sets were published in various and sometimes unclear reference frames, we invert rotation poles for each data set to minimize the residuals between these solutions and values in the International Terrestrial Reference Frame (ITRF-2005) [*Altamimi et al.*, 2007] at common fiducial stations located on the Brazil-Argentina craton (see Text S1 of the auxiliary material). Once all data sets have been rotated into ITRF-2005, we plot GPS horizontal velocities with respect to the South-American plate (as defined in the robust NNR-Nuvel1-A model [*DeMets et al.*, 1994]) by applying a rotation pole of (25.4°S, 124.6°W, 0.11°/Myr, see Figure 3).

[12] We add to these horizontal velocities the vertical velocities from the French-Chilean southern network (LiA-MdB-South [*Ruegg et al.*, 2009]). We complete this data set with vertical velocities obtained in the updated French-Chilean central data set (see Text S1 of the auxiliary material). We discarded unreliable velocities based on the following criteria: velocities based on less than 2-year time span measurements, velocities with uncertainties larger than 5.5 mm/yr or with normalized RMS (Root Mean Square) greater than 1.7, unrealistically high velocities (uplift larger than 10 mm/yr for Andean sites), velocities from survey sites that differ significantly from those of nearby cGPS stations. The final vertical velocity field includes 81 sites (Figure 4 and Table S1 in Text S2 of the auxiliary material). These selected vertical velocities are consistent with the horizontal velocity field (see Text S1 of the auxiliary material) and provide constraints for retrieving the downdip extent of the highly coupled zone [*McCaffrey*, 2002].

[13] Uncertainties are difficult to estimate and previous works differ in the manner of doing so. Some give only 1σ formal values, or rescale formal uncertainties to a conservative a-priori value, while others use complex noise models. In order to balance the weights in our inversion, we scale the published uncertainties of each data set so that their associated χ^2 value is close to 1 in our best-fitting inversions (see Text S1 of the auxiliary material and section 4). The vertical data uncertainties extracted from *Ruegg et al.* [2009] are also scaled up to a mean σ of 4 mm/yr in order to take into account the realistic errors associated with vertical GPS measurements.

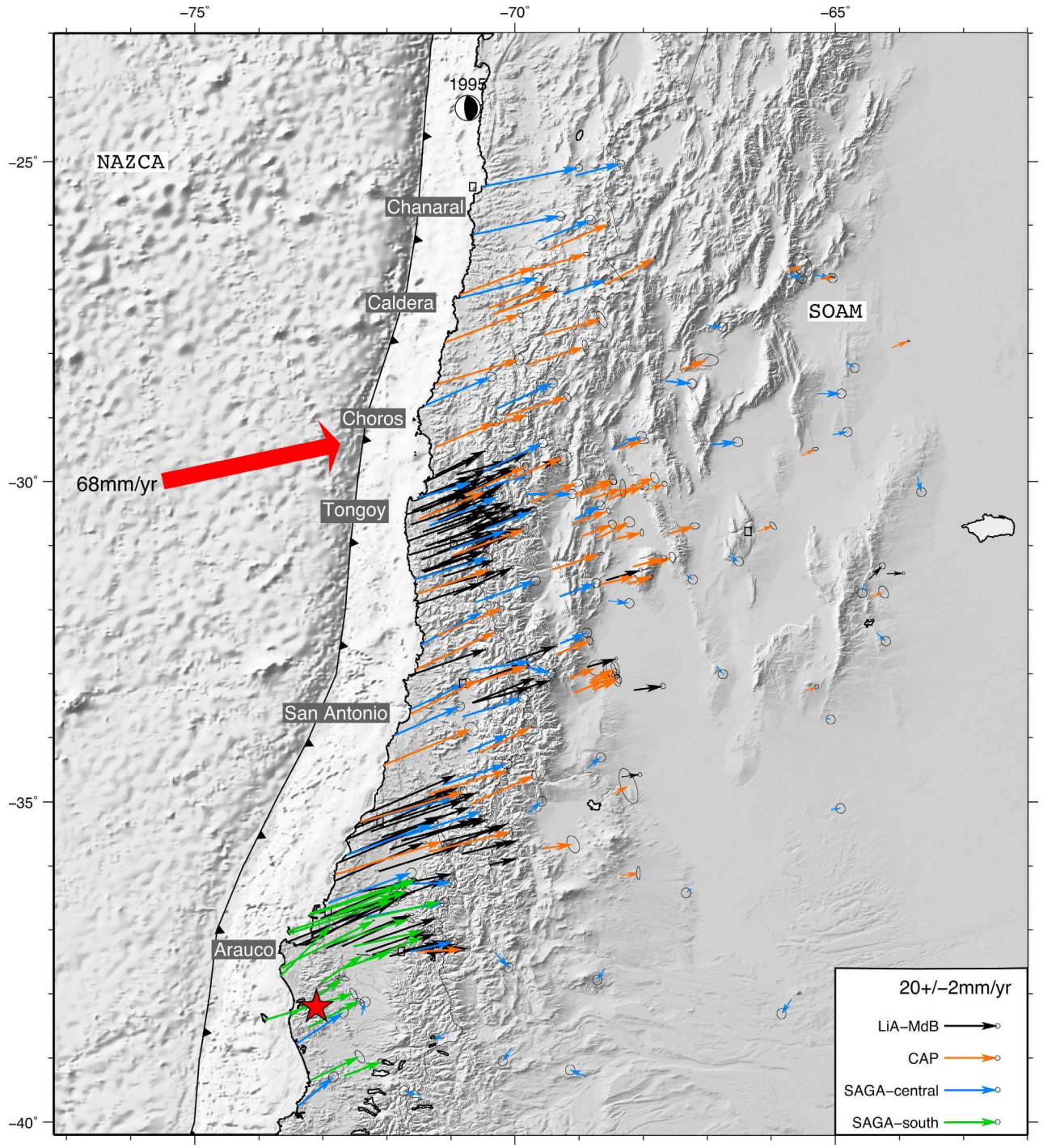

Figure 3. Final compiled data set of the upper-plate interseismic surface deformation relative to a fixed South-American plate defined by the NNR-Nuvel1A model. Different colors depict different data sets (detailed in Table S3 in Text S2 of the auxiliary material). LiA-MdB [*Ruegg et al.*, 2009; *Vigny et al.*, 2009]; CAP [*Bevis et al.*, 1999; *Brooks et al.*, 2003]; SAGA-central [*Khazaradze and Klotz*, 2003; *Klotz et al.*, 2001]; SAGA-south [*Moreno et al.*, 2008]. The hypocenter of the 1960 M_w9.5 Valdivia earthquake is plotted as a red star. The CMT focal mechanism of the 1995 Antofagasta earthquake is plotted as a beach ball. The bold red arrow shows the Nazca plate convergence with respect to the stable South America (68 mm/yr). Major coastal features are named in gray rectangles.

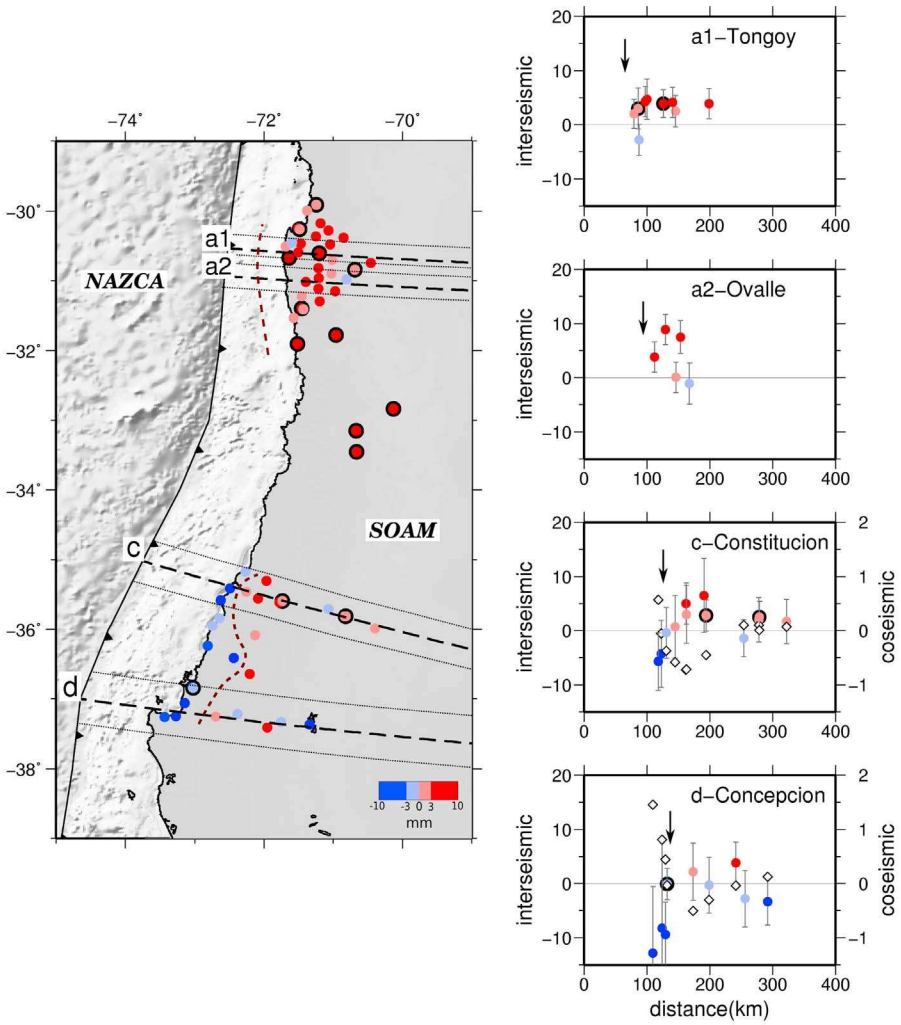

Figure 4. (left) Vertical data set used in this study. Uplift (red) and subsidence (blue) amplitudes are color coded (mm/yr). Bold contoured dots are continuous cGPS stations. Dashed profiles and dotted rectangles underline the location of the 4 profiles plotted on the right panel. Brown dashed curves indicate probable location of the hinge line. (right) Vertical deformation in mm/yr along the four profile lines plotted on the map (dashed lines). Tick marks are scaled uncertainties. Diamonds are coseismic vertical displacements in meters caused by the Maule earthquake on those profile lines. The black arrow indicates the probable location of the hinge line for each profile.

[14] This compiled data set is limited to the south by the Arauco peninsula (38°S), south of which the deformation pattern is dominated by the postseismic rebound generated by the 1960 Valdivia earthquake [*Moreno et al.*, 2008]. To the north, our data set ends at the latitude of the Chañaral peninsula (24°S), north of which the deformation pattern is affected by the 1995 Antofagasta earthquake and associated postseismic processes. The pattern of interseismic deformation defined by our horizontal and vertical velocity fields changes from south to north in central Chile. In particular, the "hinge line" (surface boundary between subsidence and uplift) is well constrained by the vertical data. South of 34°S, it is located 120 km from the trench (profiles b and c in Figure 4) and further north, it is offset 20 km closer to the trench in La Serena bay (30°S, profiles a1 and a2 in Figure 4). In addition, the horizontal deformation decreases by half from south to north (Figures 3 and 6). Together, these observations indicate along-strike variations of coupling.

4. Modeling Strategy: From Surface Deformation to Coupling Distribution

[15] During the interseismic phase of the seismic cycle, convergent plate motion generates elastic deformation in the upper plate. We invert measured interseismic surface deformation using the DEFNODE program developed by *McCaffrey* [2002], which is based on *Okada*'s [1985] solution for a buried dislocation in an elastic half-space and on the "backslip" method [*Savage*, 1983]. The "best-model" is the coupling distribution that best reproduces the surface velocity fields, i.e the model that minimizes the reduced χ^2 value (see Text S1 of the auxiliary material). We fix the rigid

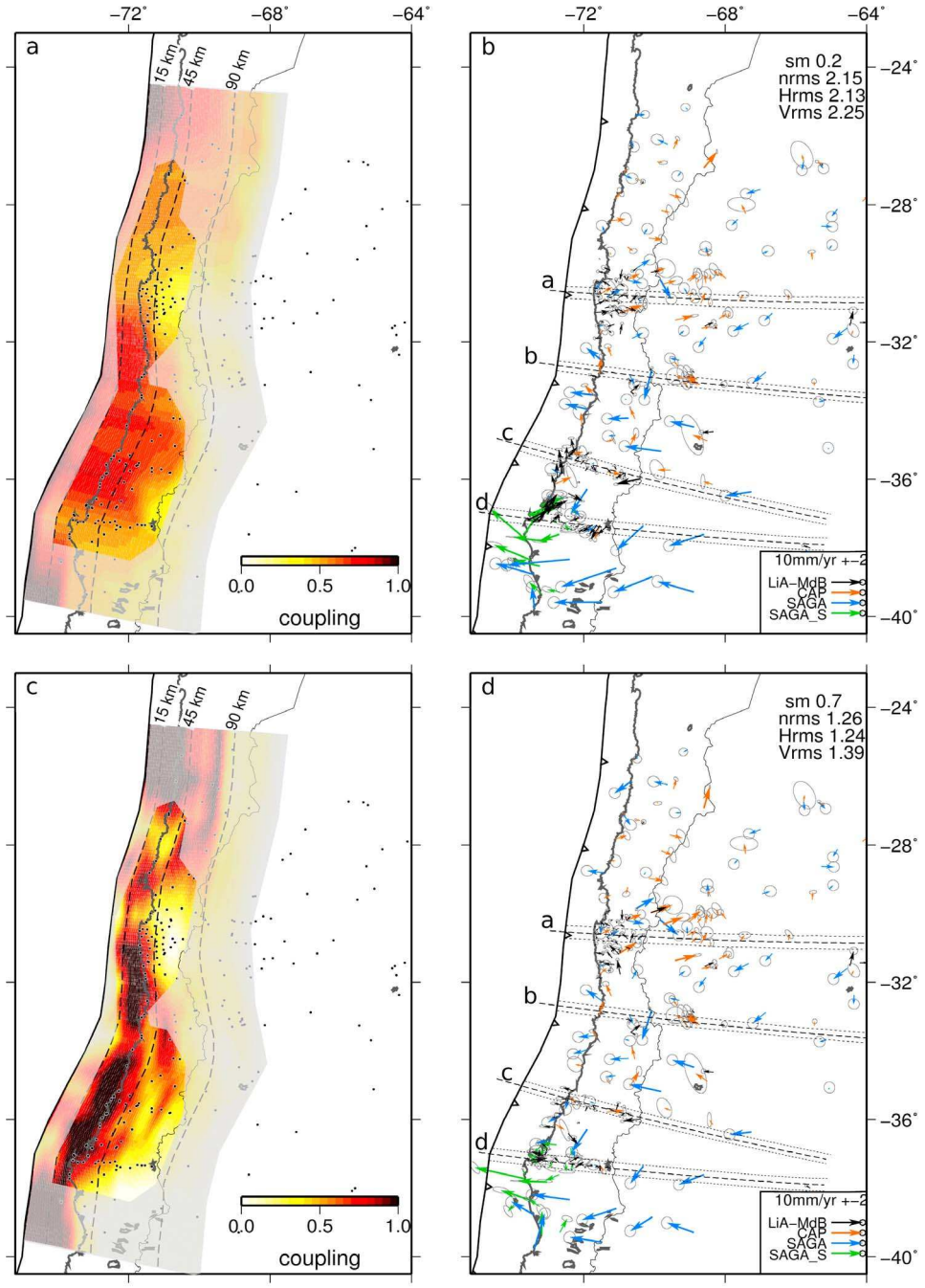

Figure 5. Coupling distributions (Figures 5a and 5c) and associated residuals (Figures 5b and 5d) of (a, b) the smoothed first-order model and (c, d) precise "best" model. Figures 5a and 5c show the coupling coefficient value (from 0% to 100%) color-coded from white to black through yellow and red. Dashed curves are slab isodepths whose values are indicated at the northern end of the slab (km). Grayish areas are poorly resolved as defined by checkerboard tests (i.e. areas where the discrepancy between the initial checkerboard coupling distribution and the inverted one is greater than 30%). Black dots show the locations of GPS sites. Figures 5b and 5d show residuals relative to each data set (color coded as in Figure 3). Dashed black lines indicate the four profiles perpendicular to the trench presented in Figure 6. They span a 20 km width area around the profile line (dashed-dotted rectangles).

rotation of the Nazca plate with respect to the South-American plate to the pole (55.9°N, 95.2°W, 0.610 °/My) published by *Vigny et al.* [2009], as it reconciles both the NNR-Nuvel1A and ITRF2005 relative poles.

[16] The interseismic coupling coefficient Φ is defined by *Hyndman et al.* [1997] and *McCaffrey* [2002] so that

$$V_{\text{interseismic}} = (1 - \Phi) V_{\text{convergence}},$$

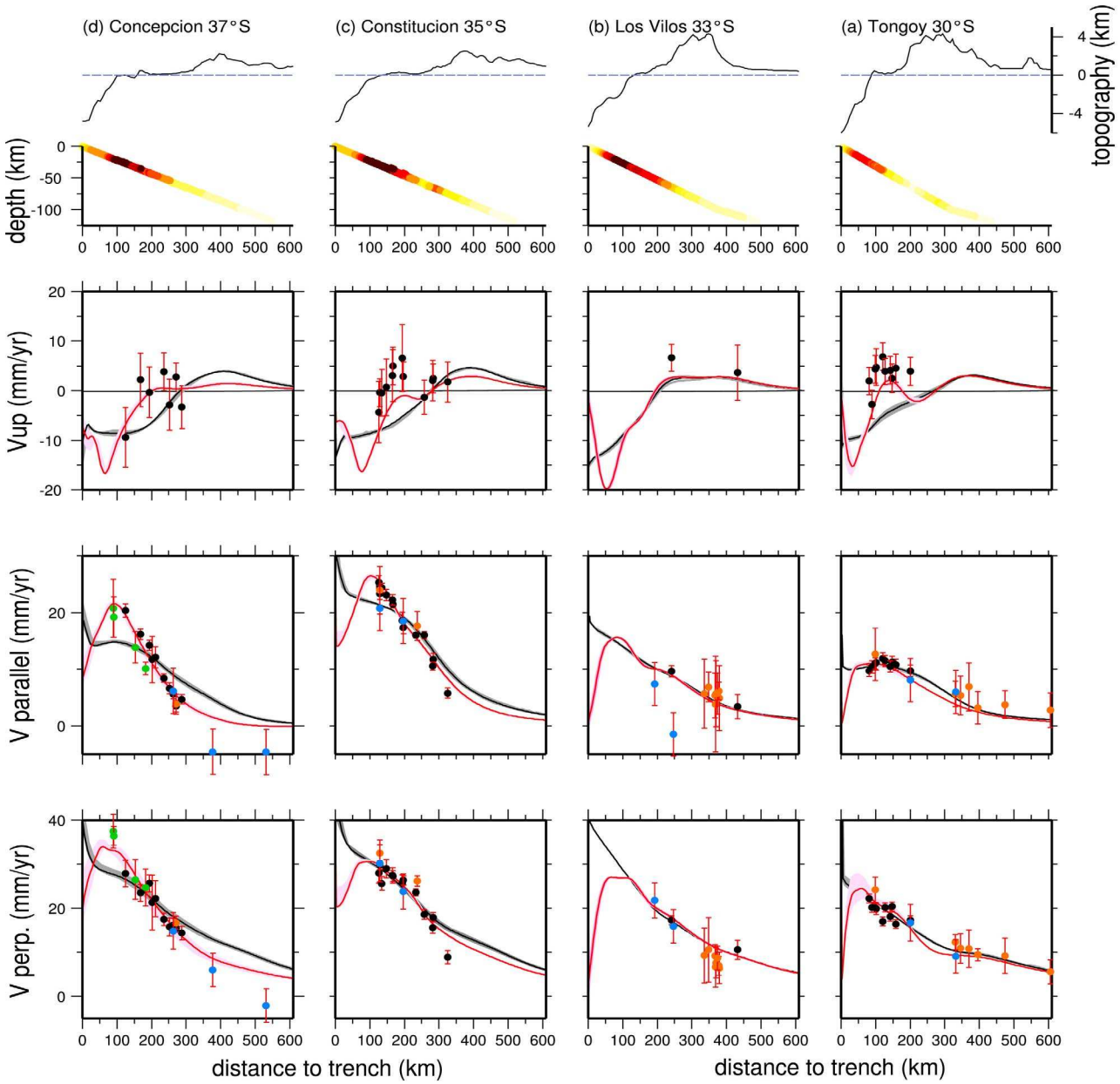

Figure 6. Fit of the smoothed first-order model (black curves) and of the second-order "best" model (pink-red curves) to the data on four 20 km width trench-normal profiles shown on Figure 5. The calculated surface deformation (in mm/yr) is plotted against the distance to the trench (in km). Because the trench is roughly North-South oriented, an increase of the "parallel to the trench" component indicates more northerly motion, while the "perpendicular to the trench" component is positive landward. The pink and gray shaded areas around the red and black plain line represent the lateral variability of the deformation of our favorite model and the first-order smooth model respectively along those 20 km wide profiles. Different colors depicts different data sets (see legend of Figure 3) plotted with their rescaled uncertainty (red tick marks). The topography (in km) and the variation with depth (in km) of the coupling coefficient in our second-order "best-model" are plotted in the upper graphs. The color code for the coupling coefficient is identical to Figure 5.

$V_{\text{interseismic}}$ being the interseismic slip rate of the interface and $V_{\text{convergence}}$ the plates convergence velocity. A 0% coupling coefficient stands for a freely creeping interface that accommodates the contemporary convergence by aseismic creep (via either steady creep or pulses of aseismic slip). On the contrary, a 100% coupling coefficient represents a locked interface that accommodates no motion during the current interseismic period and causes build-up of elastic strain in the surrounding lithosphere. Intermediate values for the coupling coefficient indicate complex zones that accommodate convergence by both seismic rupture and

creep, or spatial heterogeneity of locked patches and creeping patches.

4.1. Interface Geometry

[17] The geometry of the subduction fault used in backslip models has a crucial impact on the pattern of upper-plate deformation. In central Chile, the slab geometry has been constrained by microseismicity [*Tichelaar and Ruff*, 1991; *Pardo et al.*, 2002], gravity measurements [*Hackney et al.*, 2006], seismic profiles [*Bohm et al.*, 2002; *Asch et al.*, 2006; *Contreras-Reyes et al.*, 2010], and tomography, leading to a compiled geometry proposed by *Tassara et al.* [2006]. Despite differences depending on the authors and methodology, some large-scale features are shared by all proposed geometries. The most striking feature is the abrupt change in slab geometry between the Maule gap area (from 40°S to 34°S), where the slab invariantly dips at 15°–18°, and the northern La Serena area (from 32.5°S to 24°S). In the latter area, some authors assume a complex geometry with an average slab dip of 20° until 100 km depth followed by slab flattenning [*Pardo et al.*, 2002; *Tassara et al.*, 2006; *Hoffmann-Rothe et al.*, 2006], and other authors assume a very low (10°) dipping slab [*Vigny et al.*, 2009].

[18] In this study, we prescribe a slab geometry that is coherent with the geometry proposed by *Tassara et al.* [2006]. Our model is composed of a 15° dipping slab in the Maule gap area and of a 20° dipping plane in the La Serena area with flattening (10° dipping) beyond 100 km depth (see Figure 6). We construct a three-dimensional smooth transition between the two zones with a across-dip grid step of 0.5° and an indepth grid step of 7.5 km for the densest part of the grid. We do not take into account small perturbations induced by topographic and bathymetric effects. These may have significant effects on surface deformation near the trench where there are no measurements [*Masterlark*, 2003].

4.2. Spatial Resolution and Constraints on Inversion

[19] We conduct checkerboard tests to assess the resolution of our model (Figure S2 in Text S1 of the auxiliary material) and determine the areas where the inverted coupling coefficient differs by more than 30% from the initial forward value (gray shaded areas in Figure 5). These unresolved areas correspond to low measurement-density zones like the offshore shallowest part of the slab (0 to 15 km depth), as the GPS data set is not able to discriminate between full locking or creeping near the trench (see section 2.2 and Figure S3 in Text S1 of the auxiliary material). Coupling on the deepest parts of the plate interface (deeper than 80 km) is also poorly resolved because it generates only small-amplitude, long-wavelength variations of the surface deformation. Resolution decreases in the San Antonio area (between 33.5°S and 34.5°S) where the coast is far from the trench (∼200 km) and north of the Caldera peninsula (27.5°S), where the GPS coverage is sparse. Everywhere else, the resolution is sufficient to retrieve complex coupling patterns. In general terms, this study has more resolution than previously published ones for several reasons: (1) we combine all available data for a total of 263 GPS vectors; (2) the LiA-MdB central data set includes 30 continuous (cGPS) stations and 60 survey sites frequently remeasured (10 times over 5 years) with an average spacing of ∼25 km; (3) we use vertical displacements where they are reliable. Finally, in several specific areas where the coast comes very close to the trench (i.e., the Tongoy peninsula), the resolution is unusually good (see Text S1 of the auxiliary material).

[20] We propose in Figure 5 two coupling distributions that reasonably fit the data set, and we show alternative models in Text S1 of the auxiliary material. The first-order pattern of the data is captured by a very smoothed coupling distribution in which we impose a decrease of the coupling coefficient with depth (normalized RMS = 2.15, see Figures 5a and 5b). The details of the data set are retrieved by our "best-model" where the constraint on variability of Φ is released (normalized RMS = 1.26, see Figures 5c and 5d). In the "first-order" model, we impose an along-strike roughness coefficient of 0.2/° of latitude that decreases with depth in order to reduce numerical instabilities, whereas in our best-model, this roughness coefficient is equal to 0.7/° of latitude (see Text S1 of the auxiliary material). We estimate the uncertainty on the coupling distribution by calculating the variations of average coupling $\langle\Phi\rangle$ with latitude for every alternative model that reproduces the data with a nRMS lower than 1.5. This set of reasonable models draws an uncertainty envelope for both average coupling (Figure 8) and equivalent moment (Figure 9) of our preferred model.

5. Pattern of Interseismic Coupling

[21] The first-order smoothed model presented in Figure 5a captures the main trends of the coupling variations along trench and in depth. Nevertheless, westward systematic residuals remain, in particular in the Maule gap area. Near San Antonio(33.5°S) the coupling obtained in this first-order model is greater than shown by the data (residual arrows point toward the west, see Figure 5b). On the contrary, along the coast between Arauco and San Antonio, this smoothed model underestimates the coupling (Figure 5b). Those discrepancies are well illustrated in Figure 6 that shows the fit of this smoothed model to each velocity components on four profiles perpendicular to the trench (Concepción 37°S, Constitución 35°S, Los Vilos 33°S and Tongoy 30°S). The larger misfits are observed on the two southernmost profiles, in particular on the velocity components that are vertical and parallel to the trench. However, the data north of San Antonio (33.5°S) are well retrieved.

[22] The GPS data set, and notably the vertical components, requires more abrupt changes in the coupling distribution. Our favorite model is less smoothed and allows for both along-strike and along-dip coupling variations (Figure 5c). With the exception of the area south of Arauco (38°S) that is affected by post-seismic deformation of the 1960 earthquake, residuals are small (Nrms 1.26), below GPS formal uncertainties, and non-systematic (Figure 5 and Figure S6 in Text S1 of the auxiliary material). In this refined model, the three components of the velocities are well reproduced (Figure 6). Our results demonstrate that the upper-plate deformation in central Chile can be modeled by coupling variations on the subduction interface. The implementation of an Andean sliver rigid block, as suggested by *Brooks et al.* [2003], does not change the coupling distribution pattern. It neither improves the fit to the data (Nrms 1.28) nor reduces the residuals in the Andean and sub-Andean region. Thus the

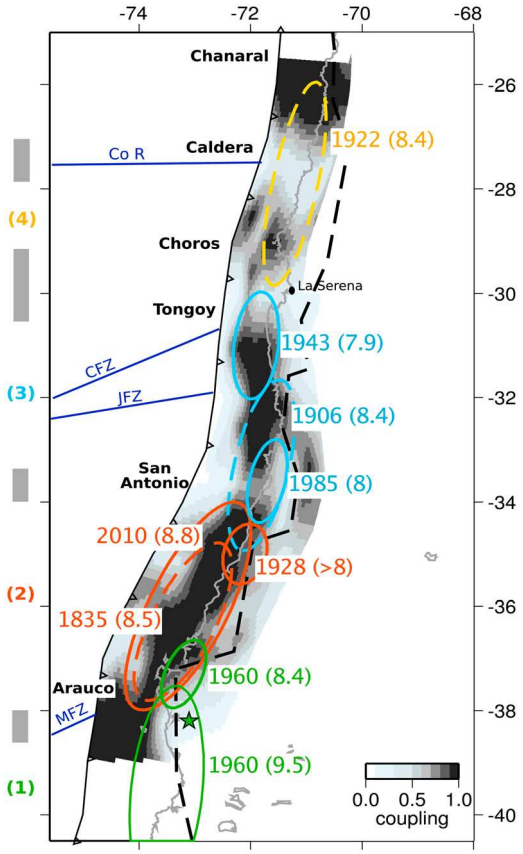

Figure 7. Coupling pattern and segmentation. Coupling distribution is color coded and superimposed by rupture zones of major instrumental or historical earthquakes (solid or dotted ellipses respectively). Dashed black line: intersection of the continental Moho with the plunging slab following *Tassara et al.* [2006]. Green star: epicenter of the 1960 M_w 9.5 earthquake (CMT). Colored ellipses depict rupture zones of major historical earthquakes that are well (solid line) or poorly (dashed line) resolved. Their color code corresponds to the segment they broke. Those segments are numbered on the left: (1) Valdivia segment (green), (2) Maule segment (red), (3) Metropolitan segment (blue), (4) Atacama segment (yellow). Grey rectangles: intersegment zones. Names of peculiar coastal features are indicated. Dark blue solid lines: bathymetric features Co R-Copiapo ridge, CFZ-Challenger fracture zone; JFR-Juan Fernandez Ridge; MFZ-Mocha Fracture Zone.

possible sliver motion is not resolvable with the available GPS data.

[23] The robust feature shared by both models, and by many alternative models presented in Text S1 of the auxiliary material, is the decrease of the coupling coefficient associated with the narrowing of the coupled zone from South to North, with a minimum in the La Serena bay, where coupling no longer exceeds 60%. Our preferred coupling model (Figures 5 and 7) shows that the highly coupled zone (Φ >70%) is generally well developed, though discontinuous, along the subduction interface. We identify three segments where coupling is intense and one segment where postseismic rebound still occurs. (1) The Valdivia segment that starts south of the Arauco peninsula (38°S) is still experiencing the postseismic deformation caused by the 1960 9.5 event [*Wang et al.*, 2007; *Moreno et al.*, 2008]. (2) The Maule segment that spreads from the Arauco peninsula (38°S) to the San Antonio bay (33.5°S) is characterized by a highly coupled zone that extends down to 45 km depth. (3) The Metropolitan segment, where the highly coupled zone narrows and where the coupling vanishes at 30 km depth, extends from San Antonio bay (33.5°S) to the Tongoy peninsula (30°S). (4) The smaller Atacama segment extends from the Choros peninsula (29.2°S) to the Caldera peninsula (27.5°S) and is characterized by a very shallow highly locked zone that is confined between the trench and 20 km depth. These segments are bounded by narrow areas where the coupling coefficient decreases sharply and where the average coupling coefficient $\langle\Phi\rangle$ (calculated for the first 60 km of the subducting slab, see Figure 8) is lower than 60%: at 38°S (South of Arauco peninsula), at 33.5°S (San Antonio bay), 30°S (La Serena bay, between Tongoy and Choros peninsulas) and 27.5°S (Caldera peninsula).

[24] The extent of the downdip transition zone, where coupling is lower than 70% and decreases with depth, also varies along-strike (roughly following the shape of the locked zone). It spreads down to 60 km in the Maule segment (from 38°S to 33.5°S) and down to 90 km (although it is poorly resolved) in the Choros to Caldera area (29.2°S to 27.5°S). The downdip transition zone narrows from San Antonio to the Tongoy Peninsula (33.5°S to 30°S) and reaches the freely creeping zone at 45 km depth only. The downdip limit of the locked zone differs from the depth of the continental Moho (Figure 7) [*Tassara et al.*, 2006]. Except in the Tongoy peninsula where the coast is not far from the trench (~70 km) and the GPS coverage is dense, we have no resolution on the shallowest part of the slab (from surface to 15 km depth) where an upper transition zone may develop (Figure S2 in Text S1 of the auxiliary material).

6. Discussion

6.1. Coupling Segmentation and Seismic Behavior

[25] Ruptures of historical large earthquakes in central Chile often stopped at intersegment areas characterized by low average coupling. They generally ruptured within the areas that are highly coupled during the interseismic period (Φ > 70%, Figures 2 and 7). The background seismicity recorded by the USGS since 1976 underlines changes in the rate and amount of moderate size earthquakes along the subduction zone. The seismicity complements the average coupling $\langle\Phi\rangle$ to define four different "coupled segments" (Figure 8). In the following, we jointly describe the interseismic coupling pattern of each segment and its seismic behavior.

[26] 1. The Valdivia segment ruptured entirely during the 1960 sequence [*Plafker and Savage*, 1970; *Cifuentes*, 1989]. Its northern limit appears to be the Arauco peninsula, a complex tectonic coastal feature, where the 1960 M_w 9.5 rupture and its M_w 8.4 foreshock nucleated, and where the Mocha Fracture Zone subducts. It is now affected by postseismic processes following this major seismic event, and the measured deformation there reflects not only interseismic

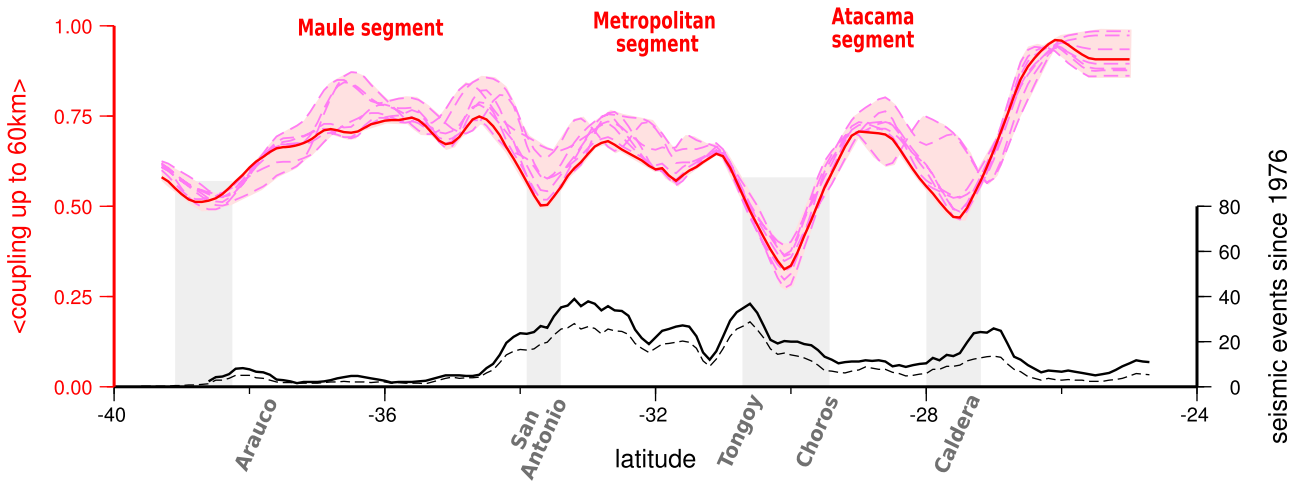

Figure 8. Average coupling coefficient versus latitude. Here $\langle\Phi\rangle$ is calculated for 0.2° sliding windows sampling the first 60 km depth of the slab for our favorite model (red bold line) and a subset of alternative models that fit the data with a nrms lower than 1.5 (dashed pink lines). The pink shaded area is the uncertainty zone of our favorite coupling distribution. Black lines indicate the number of earthquakes from the USGS catalog (1976–2009, crustal earthquakes excluded): solid line = M_w <6.5 events, z<60 km; dashed line = M_w < 5 earthquakes. Grey shaded area are the intersegment zones that bound the four "coupling segments."

loading. We therefore refrain from any interpretation of the coupling pattern in this area.

[27] 2. The Maule segment ruptured almost entirely in 1835 (from 34.9°S to 38°S [*Darwin*, 1851; *Lomnitz*, 1970; *Kelleher*, 1972]) and completely during the Maule 27 February 2010 event (M_w 8.8) [*Vigny et al.*, 2011]. We find that this area was highly coupled, with a well developed locked zone going down to 45 km depth prior to the 2010 earthquake, similar to *Ruegg et al.*'s [2009] results. The average coupling was high (>75%) in the Maule segment whereas very few moderate earthquakes occurred between 1976 and 2010 [*Campos et al.*, 2002] (Figure 8). The highly coupled zone (Φ > 100%) narrows below the Arauco peninsula, i.e. the southern boundary for this segment. The northern boundary, as visible in the coupling distribution (Figures 7, 8, and 9), is located at 33.5°S (San Antonio Bay) and corresponds to a low average coupling area. This limit corresponds to the northern extent of the 2010 Maule earthquake (Figure 9a).

[28] 3. The Metropolitan segment shows a more complex behavior. Two M_w ~8 earthquakes occurred within this segment in 1943 and 1985 [*Beck et al.*, 1998; *Comte et al.*, 1986]. An earlier larger event (the poorly studied M_w 8.4 1906 Valparaiso earthquake) ruptured its southern part and may have crossed the San Antonio barrier to the south but failed to rupture a significant length to the north [*Okal*, 2005]. To first-order, $\langle\Phi\rangle$ slightly decreases from south to north of this segment as reflected in the strain decrease observed in Figures 3 and 6. The whole segment is characterized by an unusually high intermediate-magnitude seismicity rate. Part of this seismicity probably comes from the aftershock activity following the 1985 earthquake. More specifically, $\langle\Phi\rangle$ varies along this segment and exhibits two peaks of higher coupling that may suggest the existence of two smaller asperities (Figure 8). The southern asperity may have ruptured during the 1985 and 1906 events while the northern asperity ruptured during the 1943 earthquake. This segment is affected by the subduction of two irregular bathymetric features, the Juan Fernandez ridge (JFR) and the Challenger fracture zone (CFZ) (see Figures 1 and 7). Both are correlated with a decrease of $\langle\Phi\rangle$ in Figure 8: between the two small scale asperities at 32°S, and at the northern end of the segment at 30°S. The northern boundary for this segment is La Serena bay, bounded by the Tongoy and Choros peninsulas, where the average coupling is as low as 30%.

[29] 4. The smaller Atacama segment is much less constrained by the inversion due to sparse GPS networks. It is characterized by a narrow locked zone ($\langle\Phi\rangle$ > 70%). The seismic activity in this segment since 1976 is lower than in the Metropolitan segment but still higher than in the Maule seismic gap. Although poorly defined, this segment may end to the north at the Caldera peninsula at 27.5°S. It has probably been ruptured by the 1922 (M_w 8.4) earthquake that may have extended further north than the peninsula and therefore have broken more than a single segment (Figure 7).

[30] Thus, in central Chile, interseismic loading since 1990 can be described by four "coupled segments" ($\langle\Phi\rangle$ > 70%), each of them long enough to produce a M_w~9 if they were fully locked (Figure 7). Those segments are bounded by low coupling areas ($\langle\Phi\rangle$ < 60%) that often correlate with distinct seismic behavior (a barrier to dynamic rupture propagation of major historical and instrumental earthquakes - M_w>7) and with changes in the intermediate-magnitude seismicity rate.

6.2. Mechanical Interpretation of the Interseismic Coupling Coefficient

[31] Recent publications relate the apparent coupling Φ to the spatial distribution of velocity-weakening and velocity-strengthening patches on the subduction interface [*Kaneko et al.*, 2010; *Hetland and Simons*, 2010]. According to these

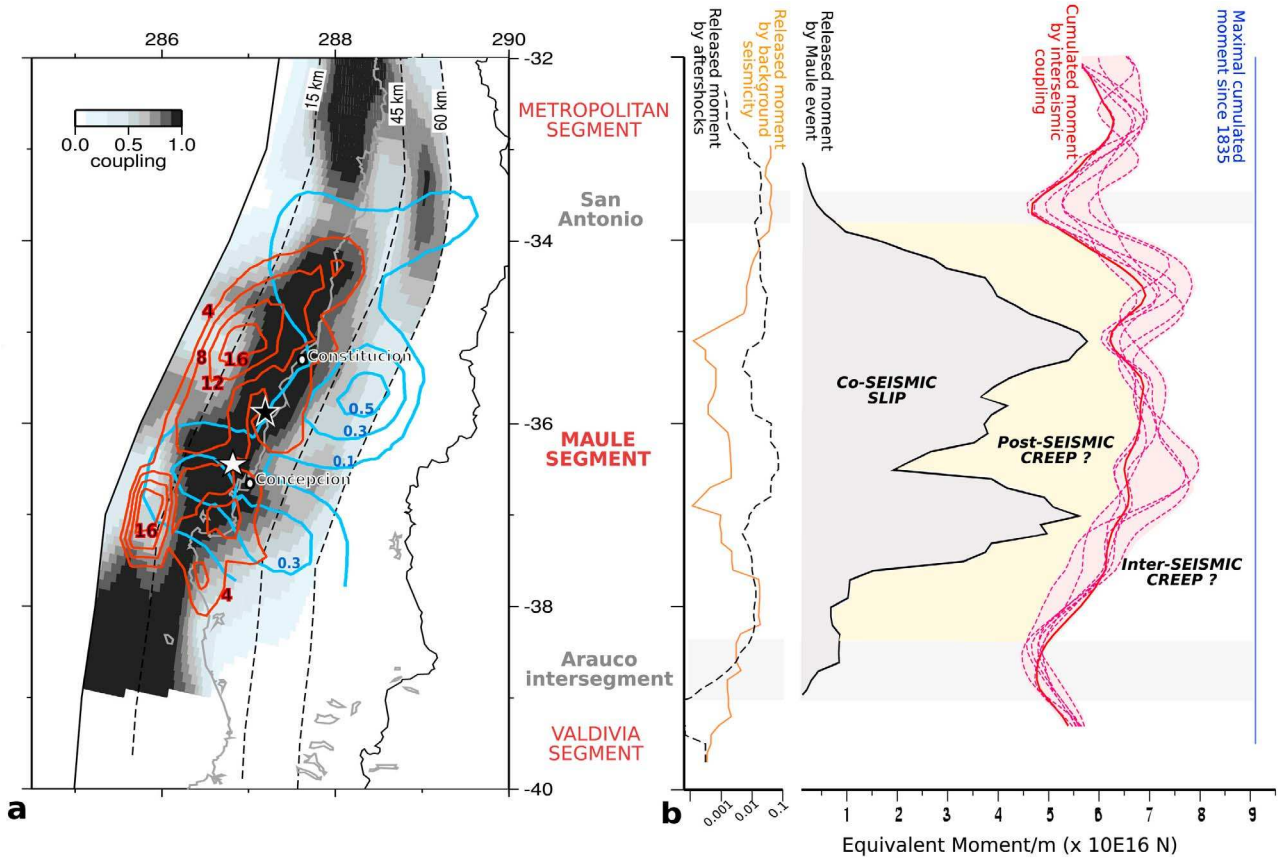

Figure 9. (a) Co-seismic slip distribution (4 m isoslip contour-lines in red) and postseismic rapid afterslip (0.2 m isoslip contour-lines in blue) [*Vigny et al.*, 2011], superimposed on our coupling distribution. White star: relocated epicenter [*Vigny et al.*, 2011]. Black star: NEIC-USGS epicenter. (b) Slip budget of the seismic cycle along the Maule segment (segment 2). Moment scale is $\times 10^{16}$N per meter of subduction. The released or cumulated moment is calculated for the first 232 km of the slab (i.e from 0 to 60 km depth for a 15° dipping slab). Blue line: maximal local moment accumulated since 1835; red plain curve: local moment accumulated by elastic deformation during the interseismic phase of the cycle (best model). Pink shaded area: uncertainty of our favorite coupling model. Black solid line: moment released by the Maule event [*Vigny et al.*, 2011]. Dashed black curve: moment released per subduction unit by the first month of aftershock, excepting the Pichilemu M_w 6.8 aftershock (USGS). Orange plain curve: moment released by the intermediate magnitude seismicity from 1990 until the Maule event. Grey shaded areas: intersegment zones.

studies, the value of Φ depends on the number, size and spacing of velocity-weakening asperities.

[32] To first-order, the highly locked zones (Φ > 70%, i.e close to full locking), can be interpreted as velocity-weakening asperities that may rupture during the coseismic phase, although small-scale velocity-strengthening areas may be hidden in the stress shadow of neighboring velocity-weakening asperities. The intersegment areas, characterized by a lower apparent coupling coefficient, can reflect either a velocity-strengthening patch surrounded by two large velocity-weakening asperities [e.g., *Kaneko et al.*, 2010], or a patchwork of very small scale velocity-weakening asperities that may produce small-magnitude seismicity surrounded by creep during the interseismic phase [e.g., *Hetland and Simons*, 2010]. Both scenarios involve a simple relationship between the amplitude of the apparent coupling coefficient and the spacing between neighboring velocity-weakening asperities: the larger the spacing, the lower the coupling. We observe the same kind of relation in the Chilean case. In the large La Serena intersegment zone (between Tongoy and Choros peninsulas, see Figure 8) that extends over ∼100 km along strike, ⟨Φ⟩ decreases to 30% at the center of the barrier. Note that this is independent of the roughness coefficient applied to the inversion (Figure 8). In the Caldera intersegment area (about 80 km wide) it reaches 46%, and in the narrow San Antonio intersegment area (less than 50 km width) ⟨Φ⟩ reaches 50% or more depending on the roughness coefficient used. *Kaneko et al.* [2010] also demonstrate that a wide velocity-strengthening area (between two velocity-weakening asperities) with low apparent coupling coefficient has a high probability of acting as a barrier to rupture propagation. The wider the area and the lower the apparent coupling, the higher this probability. This idea seems to match the historical seismicity of Chile reported since the 16th century (Figure 2).The widest intersegment area is the La Serena

bay area (from Tongoy to Choros peninsulas), which stopped several major events (1730, 1819, 1880, 1922 and 1943 events), while no recorded event since the 16th century seems to have propagated through it (Figure 2). In contrast, the narrow San Antonio barrier that stopped the Maule event only stopped two historical earthquakes, in 1822 and 1851, while several major ruptures propagated through it (1730, 1647 and possibly 1906 events).

[33] These four intersegment zones exhibit a rate of background seismicity (interplate or intraslab events) that is generally higher than in the coupled segments (Figure 8). This could be compatible with interfingering of velocity-strengthening patches (prone to creep) with small-scale stick-slip asperities that would be continuously charged by the surrounding interseismic creep. In this case, between large megathrust earthquakes, these low coupling areas may creep with an associated microseismicity rather than accumulate elastic deformation. Those barriers should be regarded as places where the subduction accommodates the convergence by a combination of intermediate magnitude seismic swarms and creep. However, so far, no transient creep pulses have been detected in those areas.

6.3. Tectonics of Intersegment Zones

[34] The four intersegment zones defined in this work are often associated with coastal features like bays, peninsulas, or faulting of the continental crust and less often with subduction of bathymetric features such as fracture zones or topographic highs (Figures 1 and 7). A similar correlation has been made in other subduction zones: (1) in the Nazca-South America subduction, the Pisco peninsula where the Nazca ridge subducts, correlates with a decrease in interseismic coupling and with a zone that acts as a barrier for great earthquakes [*Perfettini et al.*, 2005, 2010]; (2) in the Nankai trench, the Kii peninsula is associated with low coupling, with the subduction of an oceanic fracture zone, and correlates with a barrier for seismic events [*Cummins et al.*, 2002]; (3) in the Sumatra subduction, Batu island correlates with the subduction of the Investigator fracture zone and constitutes a very low coupling zone between two major asperities that can be considered as a barrier for several seismic events [*Konca et al.*, 2008].

[35] Several mechanisms can be invoked to support such correlations. First, the subduction of major bathymetric features can modify the normal stress which in turn affects fluid pressure on the megathrust interface [*Liu and Rice*, 2005; *Reyners and Eberhart-Phillips*, 2009; *Sparkes et al.*, 2010], or modify the slab bending and fracturing of the plates in contact [*Wang and Bilek*, 2011]. Those effects can play an important role in the existence of the La Serena and Arauco barriers, where bathymetric features (CFZ and MFZ) subduct (Figures 1 and 7). Subduction of bathymetric features may be the primary factor, since the barriers seem to be the most efficient in this case. Second, geometrical complexities can damage the upper plate, generate crustal faults networks and affect the mechanical behavior of the interface [*Armijo and Thiele*, 1990; *Melnick and Bookhagen*, 2009]. This may concern at least the Arauco peninsula and the Mejillones peninsula in North Chile (23°S) [*Béjar-Pizarro et al.*, 2009; *Motagh et al.*, 2010; *Comte et al.*, 2010]. Third, the change in obliquity of the trench may produce geometrical boundaries that affect rupture propagation. It is possible that those areas undergo a local accumulation of strain that cannot be released by typical subduction events for a certain amount of time.

6.4. From Interseismic Loading to Seismic Rupture and Aseismic Transient Slip: The Case of the Maule Segment

[36] Three lines of evidence suggested that the Maule segment was near failure before the 2010 event: (i) unusually low seismic activity since at least 1976 [*Campos et al.*, 2002], (ii) intense elastic deformation of the upper-plate revealing high coupling of the subduction interface [*Ruegg et al.*, 2009], (iii) and 175 years of latency since the last major earthquake with up to 12 m of accumulated slip deficit, assuming full coupling of the interface. The Maule rupture that occurred on February 27th 2010 (M_w 8.8), broke the area that was interseismically coupled with $\Phi > 70\%$ (see Figure 9) [*Vigny et al.*, 2011].

[37] The patches of highest coseismic slip in the model of *Vigny et al.* [2011] correlate to zones of high coupling in our interseismic coupling model. Both ends of the rupture correspond to areas where the locked zone vanishes (San Antonio, 33.5°S) or narrows (south of Arauco peninsula, 38°S) and where both the average coupling coefficient and the amount of coseismic slip decrease (Figure 9). The lesser slip area (i.e. the area corresponding to a local coseismic slipminimum, from 36.2°S to 36.7°S) that separates the two main coseismic slip asperities (35°S and 37°S), does not appear in the coupling distribution. More specifically, the coseismic motion measured by GPS requires more than 15 m of coseismic slip in the shallowest zone of the interface where the resolution of our interseismic model is poor: it is therefore difficult to assert whether there is a correlation between coupling and coseismic slip in this area. One can therefore not rule out the hypothesis that this shallow coseismic slip may have been accumulated by elastic deformation during the interseismic phase.

[38] The early post-seismic signal reported by *Vigny et al.* [2011] mostly occurred in the downdip transition zone (with a maximum slip of 0.6 m over 12 days) and at the northern end of the rupture. These two areas correspond to intermediate to low interseismic coupling zones where $\langle\Phi\rangle < 60\%$ (Figure 9). On the other hand, significant postseismic slip also occurred in the lesser coseismic slip region, where the apparent coupling is close to 100%.

[39] Several important conclusions result from this comparison. First, as previously shown by *Moreno et al.* [2010] and to first-order, the latitudinal extension of high coupling zones ($\Phi > 70\%$) correlates well with the extent of the zones that experience significant slip during the co-seismic phase. Second, intermediate coupling zones are correlated either along the trench and in depth, with zones that experience less coseismic slip and that could stop the dynamic rupture propagation. Third, those intermediate coupling zones experience significant postseismic transient slip.

[40] Nevertheless, the correlation between highly coupled interseismic areas and high slip co-seismic patches is far from perfect. The lesser slip area (from 36.2°S to 36.7°S) located between the two main coseismic slip asperities, experienced both coseismic slip and important postseismic afterslip and is a good example of this imperfection. Following *Hetland and Simons* [2010], we conclude that this

area might be made of isolated velocity-strengthening patches surrounded by numerous velocity-weakening asperities. The former would appear artificially locked by the neighboring velocity-weakening asperities and unable to creep during the interseismic period, leading to an apparent coupling coefficient close to 100%. The rupture of the surrounding locked asperities would enable stress loading and result in triggered post-seismic creep [*Hetland and Simons*, 2010]. Such narrow areas located in the stress shadow of large locked asperities have been identified in the Sumatra trench after the Mentawai 2007 earthquake [*Konca et al.*, 2008], but also in the Peruvian part of the Nazca-South America subduction trench after the Pisco earthquake. There, *Sladen et al.* [2010] and *Perfettini et al.* [2010] showed that the zone of limited slip between the two major coseismic slip patches was not detected in the interseismic coupling distribution and appeared as an intermediate to high coupling zone.

[41] Furthermore, the lesser-coseismic slip area in the Maule earthquake underwent a high rate of aftershocks in the first month following the main shock corresponding to an important moment release (Figure 9), as previously observed in the case of the Pisco earthquake [*Sladen et al.*, 2010]. This area also experienced a M_w 6.8 earthquake that occurred on February 11th of 2011 and that is one of the largest aftershocks recorded for this earthquake. On the contrary, fewer aftershocks occurred within the main coseismic slip areas. The distribution of the moment released by aftershocks is thus consistent with the distribution of moment released by background seismicity during the interseismic loading phase (Figure 9). The moment released by seismicity is obtained assuming that the present seismicity rate (inferred over 30 years from the NEIC-USGS catalogue) has been constant since 1835. This correlation suggests that (1) the same small scale velocity-weakening asperities may rupture during both phases of the seismic cycle, (2) the main coseismic asperities correspond to large velocity-weakening areas, and (3) the lesser coseismic slip area in between is a patchy zone of the subduction interface composed of both velocity-weakening and velocity-strengthening patches that experience relatively more aftershocks and background seismicity than the neighboring large velocity-weakening asperities that rupture during megathrust earthquakes only.

[42] If the coupling were homogeneous and equal to 100% everywhere along the Maule segment, the cumulative moment over the entire interseismic period (from 1835 to 2010) would have been $\sim 4.0 \times 10^{22}$ Nm. Assuming that the coupling pattern deduced from 10 years of GPS measurement prevailed over this period, we find a reduced cumulated moment of 2.8×10^{22} Nm (i.e 70% of the fully locked cumulative moment). The remaining 30% should have been released mainly by aseismic creep while less than 1% was released by intermediate-magnitude seismicity during the interseismic period. This interseismic creep component is low compared to the estimates of *Perfettini et al.* [2010] in the Peru megathrust where it accounts for 41 to 62% of the long term interplate slip. Using the slip-distribution model for the Maule event of *Vigny et al.* [2011] we estimate the moment released by the coseismic rupture (Figure 9). The Maule main shock moment is 1.73×10^{22}N.m, implying that the coseismic rupture of the Maule segment released on average 60% of the cumulated moment caused by elastic strain accumulation during the interseismic period, while the contribution of aftershocks is negligible. In front of Constitución (35°S) and Concepción (37°S), the moment released by coseismic slip reaches ∼88% of the accumulated moment during interseismic loading.

7. Conclusion

[43] We demonstrate in this study that it is possible to fit the interseismic deformation pattern along the South-America and Nazca plate boundary in central Chile (38°S to 24°S), with a simple elastic model of a locked subduction interface with varying coupling, both along strike and dip. An important consequence is that neither secondary faults nor tectonic sliver are needed to explain the surface deformation field at these latitudes. Our data do not rule out their existence, but imply that if they exist, the current GPS configuration can not detect them. The best model obtained for a simple geometry of the plate interface shows significant along-strike variations in the amount of coupling and extent of both the highly coupled zone and the downdip transition zone, as well as along-dip variations. Wide highly coupled areas (average coupling lower than 70%) separated by narrow zones of low coupling define four segments that correlate with the seismic history of central Chile. Narrow intersegment zones where the mean coupling is lower than 60% are associated with subduction of major bathymetric features (ridges or fracture zones), changes in thrust orientations and/or local continental fault systems associated with coastal peninsulas. The wider and the less coupled those intersegment zones are, the more likely they are to stop large earthquake ruptures.

[44] The Maule segment, where the 27th February 2010 M_w 8.8 earthquake occurred, was one of these highly coupled areas. The lateral extent and downdip limit of the Maule's coseismic slip distribution correlate with the coupling pattern that prevailed there before the earthquake. At both ends, the rupture was stopped by the presence of low coupling areas. The rapid postseismic aseismic motion and major aftershocks following this event occurred preferentially in areas where the interseismic coupling was low. The analysis of this megathrust event and of the interseismic coupling distribution enables us to propose a first-order relation between the apparent kinematic coupling parameter and the mechanical behavior of the interface during the interseismic, coseismic and postseismic phases of the seismic cycle. This apparent coupling, Φ, can thus be regarded as a proxy for the spatial distribution of velocity-weakening and velocity-strengthening patches on the subduction plane that can be combined with detailed seismotectonic studies to help assess seismic hazard along subduction zones.

[45] **Acknowledgments.** This work was performed in the frame of the French-Chilean LiA "Montessus de Ballore" with financial support of the ANR. We would like to thank R. McCaffrey for freely providing the DEFNODE code. Most figures of this paper were generated using the free Generic Mapping Tools software (GMT). We would like to thank R. Madariaga, R. Armijo, P. Bernard, and R. Grandin for constructive discussions; anonymous reviewers for a very thorough and constructive review; and the whole LIA team for its support. Special thanks to Wayne Crawford for his thorough editing of our paper. This is IPGP contribution 3268.

References

Altamimi, Z., X. Collilieux, J. Legrand, B. Garayt, and C. Boucher (2007), ITRF2005: A new release of the International Terrestrial Reference Frame based on time series of station positions and Earth Orientation Parameters, *J. Geophys. Res.*, *112*, B09401, doi:10.1029/2007JB004949.

Armijo, R., and R. Thiele (1990), Active faulting in northern Chile: Ramp stacking and lateral decoupling along a subduction plate boundary?, *Earth Planet. Sci. Lett.*, *98*(1), 40–61.

Asch, G., et al. (2006), Seismological studies of the central and southern Andes, in *The Andes: Active Subduction Orogeny*, pp. 443–457, Springer, Berlin.

Audin, L., P. Lacan, H. Tavera, and F. Bondoux (2008), Upper plate deformation and seismic barrier in front of Nazca subduction zone: The Chololo Fault System and active tectonics along the Coastal Cordillera, southern Peru, *Tectonophysics*, *459*(1–4), 174–185.

Beck, S., S. Barrientos, E. Kausel, and M. Reyes (1998), Source characteristics of historic earthquakes along the central Chile subduction Askew et Alzone, *J. South Am. Earth Sci.*, *11*(2), 115–129.

Béjar-Pizarro, M., et al. (2009), Asperities and barriers on the seismogenic zone in North Chile: State-of-the-art after the 2007 M_w 7.7 Tocopilla earthquake inferred by GPS and InSAR data, *Geophys. J. Int.*, *183*, 390–406.

Bevis, M., E. C. Kendrick, R. Smalley Jr, T. Herring, J. Godoy, and F. Galban (1999), Crustal motion north and south of the Arica deflection: Comparing recent geodetic results from the central Andes, *Geochem. Geophys. Geosyst.*, *1*(12), 1005, doi:10.1029/1999GC000011.

Bevis, M., E. Kendrick, R. Smalley Jr, B. Brooks, R. Allmendinger, and B. Isacks (2001), On the strength of interplate coupling and the rate of back arc convergence in the central Andes: An analysis of the interseismic velocity field, *Geochem. Geophys. Geosyst.*, *2*(11), 1067, doi:10.1029/2001GC000198.

Biggs, J., and D. P. Robinson (2009), The 2007 Pisco, Peru, earthquake (M8. 0): Seismology and geodesy, *Geophys. J. Int.*, *176*(3), 657–669.

Bohm, M., S. Luth, H. Echtler, G. Asch, K. Bataille, C. Bruhn, A. Rietbrock, and P. Wigger (2002), The southern Andes between 36 and 40 S latitude: Seismicity and average seismic velocities, *Tectonophysics*, *356*(4), 275–289.

Brooks, B. A., M. Bevis, R. Smalley Jr, E. Kendrick, R. Manceda, E. Lauría, R. Maturana, and M. Araujo (2003), Crustal motion in the southern Andes (26–36 S): Do the Andes behave like a microplate?, *Geochem. Geophys. Geosyst.*, *4*(10), 1085, doi:10.1029/2003GC000505.

Campos, J., D. Hatzfeld, R. Madariaga, G. López, E. Kausel, A. Zollo, G. Iannacone, R. Fromm, S. Barrientos, and H. Lyon-Caen (2002), A seismological study of the 1835 seismic gap in south-central Chile, *Phys. Earth Planet. Inter.*, *132*(1–3), 177–195.

Chlieh, M., J. B. De Chabalier, J. C. Ruegg, R. Armijo, R. Dmowska, J. Campos, and K. L. Feigl (2004), Crustal deformation and fault slip during the seismic cycle in the North Chile subduction zone, from GPS and InSAR observations, *Geophys. J. Int.*, *158*(2), 695–711.

Cifuentes, I. L. (1989), The 1960 Chilean earthquakes, *J. Geophys. Res.*, *94*(B1), 665–680.

Comte, D., and M. Pardo (1991), Reappraisal of great historical earthquakes in the northern Chile and southern Peru seismic gaps, *Nat. Hazards*, *4*(1), 23–44.

Comte, D., A. Eisenberg, E. Lorca, M. Pardo, L. Ponce, R. Saragoni, S. K. Singh, and G. Suárez (1986), The 1985 central Chile earthquake: A repeat of previous great earthquakes in the region?, *Science*, *233*(4762), 449–453.

Comte, D., M. Farías, S. Roecker, D. Carrizo, and M. H. Pardo (2010), Crustal normal faulting triggered by the M_w = 8.8 Maule megathrust subduction earthquake in central Chile, Abstract G33A-0816 presented at 2010 Fall Meeting, AGU, San Francisco, Calif., 13–17 Dec.

Contreras-Reyes, E., E. R. Flueh, and I. Grevemeyer (2010), Tectonic control on sediment accretion and subduction off south central Chile: Implications for coseismic rupture processes of the 1960 and 2010 megathrust earthquakes, *Tectonics*, *29*, TC6018, doi:10.1029/2010TC002734.

Cummins, P. R., T. Baba, S. Kodaira, and Y. Kaneda (2002), The 1946 Nankai earthquake and segmentation of the Nankai Trough, *Phys. Earth Planet. Inter.*, *132*(1–3), 75–87.

Darwin, C. (1851), *Geological Observation on Coral Reefs, Volcanic Islands and on South America*, Smith Elder, London.

Delouis, B., J. M. Nocquet, and M. Vallée (2010), Slip distribution of the February 27, 2010 M_w = 8.8 Maule earthquake, central Chile, from static and high-rate GPS, InSAR, and broadband teleseismic data, *Geophys. Res. Lett.*, *37*, L17305, doi:10.1029/2010GL043899.

DeMets, C., R. G. Gordon, D. F. Argus, and S. Stein (1994), Effect of recent revisions to the geomagnetic reversal timescale on estimates of current plate motions, *Geophys. Res. Lett.*, *21*(20), 2191–2194.

Fitch, T. J. (1972), Plate convergence, transcurrent faults, and internal deformation adjacent to southeast Asia and the western Pacific, *J. Geophys. Res.*, *77*, 4432–4460.

Hackney, R. I., et al. (2006), The segmented overriding plate and coupling at the south-central Chilean margin (36–42 S), in *The Andes: Active Subduction Orogeny*, pp. 355–374, Springer, Berlin.

Hetland, E. A., and M. Simons (2010), Post-seismic and interseismic fault creep II: Transient creep and interseismic stress shadows on megathrusts, *Geophys. J. Int.*, *181*(1), 99–112.

Hoffmann-Rothe, A., N. Kukowski, G. Dresen, H. Echtler, O. Oncken, J. Klotz, E. Scheuber, and A. Kellner (2006), Oblique convergence along the Chilean margin: Partitioning, margin-parallel faulting and force interaction at the plate interface, in *The Andes: Active Subduction Orogeny*, pp. 125–146, Springer, Berlin.

Hyndman, R. D., M. Yamano, and D. A. Oleskevich (1997), The seismogenic zone of subduction thrust faults, *Isl. Arc*, *6*(3), 244–260.

Ide, S., A. Baltay, and G. C. Beroza (2011), Shallow dynamic overshoot and energetic deep rupture in the 2011 Mw 9.0 Tohoku-Oki earthquake, *Science*, *332*(6036), 1426–1429.

Kaneko, Y., J. P. Avouac, and N. Lapusta (2010), Towards inferring earthquake patterns from geodetic observations of interseismic coupling, *Nat. Geosci.*, *3*, 363–369.

Kelleher, J. A. (1972), Rupture zones of large South American earthquakes and some predictions, *J. Geophys. Res.*, *77*(11), 2087–2103.

Kendrick, E., M. Bevis, R. J. Smalley, and B. Brooks (2001), An integrated crustal velocity field for the central Andes, *Geochem. Geophys. Geosyst.*, *2*(11), 1066, doi:10.1029/2001GC000191.

Khazaradze, G., and J. Klotz (2003), Short-and long-term effects of GPS measured crustal deformation rates along the south central Andes, *J. Geophys. Res.*, *108*(B6), 2289, doi:10.1029/2002JB001879.

Klotz, J., G. Khazaradze, D. Angermann, C. Reigber, R. Perdomo, and O. Cifuentes (2001), Earthquake cycle dominates contemporary crustal deformation in central and southern Andes, *Earth Planet. Sci. Lett.*, *193*(3–4), 437–446.

Konca, A. O., et al. (2008), Partial rupture of a locked patch of the Sumatra megathrust during the 2007 earthquake sequence, *Nature*, *456*(7222), 631–635.

Lay, T., C. J. Ammon, H. Kanamori, K. D. Koper, O. Sufri, and A. R. Hutko (2010), Teleseismic inversion for rupture process of the 27 February 2010 Chile (M_w 8.8) earthquake, *Geophys. Res. Lett.*, *37*, L13301, doi:10.1029/2010GL043379.

Liu, Y., and J. R. Rice (2005), Aseismic slip transients emerge spontaneously in three-dimensional rate and state modelling of subduction earthquake sequences, *J. Geophys. Res.*, *110*, B08307, doi:10.1029/2004JB003424.

Lomnitz, C. (1970), Major earthquakes and tsunamis in Chile during the period 1535 to 1955, *Int. J. Earth Sci.*, *59*(3), 938–960.

Masterlark, T. (2003), Finite element model predictions of static deformation from dislocation sources in a subduction zone: Sensitivities to homogeneous, isotropic, Poisson-solid, and half-space assumptions, *J. Geophys. Res.*, *108*(B11), 2540, doi:10.1029/2002JB002296.

McCaffrey, R. (2002), Crustal block rotations and plate coupling, in *Plate Boundary Zones*, *Geodyn. Ser*, vol. 30, edited by S. Stein and J. T. Freymueller, pp. 101–122, AGU, Washington, D. C.

Melnick, D., and B. Bookhagen (2009), Segmentation of megathrust rupture zones from fore-arc deformation patterns over hundreds to millions of years, Arauco peninsula, Chile, *J. Geophys. Res.*, *114*, B01407, doi:10.1029/2008JB005788.

Moreno, M. S., J. Klotz, D. Melnick, H. Echtler, and K. Bataille (2008), Active faulting and heterogeneous deformation across a megathrust segment boundary from GPS data, south central Chile (36–39 S), *Geochem. Geophys. Geosyst.*, *9*, Q12024, doi:10.1029/2008GC002198.

Moreno, M. S., M. Rosenau, and O. Onken (2010), 2010 Maule earthquake slip correlates with pre-seismic locking of Andean subduction zone, *Nature*, *467*, 198–202.

Motagh, M., B. Schurr, J. Anderssohn, B. Cailleau, T. R. Walter, R. Wang, and J. P. Villotte (2010), Subduction earthquake deformation associated with 14 November 2007, M_w 7.8 Tocopilla earthquake in Chile: Results from InSAR and aftershocks, *Tectonophysics*, *490*, 60–68.

Muller, R. D., W. R. Roest, J. Y. Royer, L. M. Gahagan, and J. G. Sclater (1997), Digital isochrons of the world's ocean floor, *J. Geophys. Res.*, *102*(B2), 3211–3214.

Nishenko, S. P. (1991), Circum-Pacific seismic potential: 1989–1999, *Pure Appl. Geophys.*, *135*(2), 169–259.

Norabuena, E., L. Leffler-Griffin, A. Mao, T. Dixon, S. Stein, I. S. Sacks, L. Ocola, and M. Ellis (1998), Space geodetic observations of Nazca-South America convergence across the central Andes, *Science*, *279*(5349), 358–362.

Okada, Y. (1985), Surface deformation due to shear and tensile faults in a half-space, *Bull. Seismol. Soc. Am.*, *75*(4), 1135–1154.

Okal, E. A. (2005), A re-evaluation of the great Aleutian and Chilean earthquakes of 1906 August 17, *Geophys. J. Int.*, *161*(2), 268–282.

Oleskevich, D. A., R. D. Hyndman, and K. Wang (1999), The updip and downdip limits to great subduction earthquakes: Thermal and structural models of Cascadia, south Alaska, SW Japan, and Chile, *J. Geophys. Res.*, *104*(B7), 14965–14991.

Pardo, M., D. Comte, and T. Monfret (2002), Seismotectonic and stress distribution in the central Chile subduction zone, *J. South Am. Earth Sci.*, *15*(1), 11–22.

Perfettini, H., J. P. Avouac, and J. C. Ruegg (2005), Geodetic displacements and aftershocks following the 2001 M_w = 8.4 Peru earthquake: Implications for the mechanics of the earthquake cycle along subduction zones, *J. Geophys. Res.*, *110*, B09404, doi:10.1029/2004JB003522.

Perfettini, H., et al. (2010), Seismic and aseismic slip on the central Peru megathrust, *Nature*, *465*(7294), 78–81.

Peyrat, S., R. Madariaga, E. Buforn, J. Campos, G. Asch, and J. P. Vilotte (2010), Kinematic rupture process of the 2007 Tocopilla earthquake and its main aftershocks from teleseismic and strong-motion data, *Geophys. J. Int.*, *182*, 1411–1430.

Plafker, G., and J. C. Savage (1970), Mechanism of the Chilean earthquakes of May 21 and 22, 1960, *Geol. Soc. Am. Bull.*, *81*(4), 1001–1030.

Pritchard, M. E., and M. Simons (2006), An aseismic slip pulse in northern Chile and along-strike variations in seismogenic behavior, *J. Geophys. Res.*, *111*, B08405, doi:10.1029/2006JB004258.

Reyners, M., and D. Eberhart-Phillips (2009), Small earthquakes provide insight into plate coupling and fluid distribution in the Hikurangi subduction zone, New Zealand, *Earth Planet. Sci. Lett.*, *282*(1–4), 299–305.

Ruegg, J. C., et al. (1996), The M_w = 8.1 Antofagasta (North Chile) earthquake of July 30, 1995: First results from teleseismic and geodetic data, *Geophys. Res. Lett.*, *23*(9), 917–920.

Ruegg, J. C., A. Rudloff, C. Vigny, R. Madariaga, J. B. De Chabalier, J. Campos, E. Kausel, S. Barrientos, and D. Dimitrov (2009), Interseismic strain accumulation measured by GPS in the seismic gap between Constitución and Concepción in Chile, *Phys. Earth Planet. Inter.*, *175*(1–2), 78–85.

Ruff, L., and H. Kanamori (1983), Seismic coupling and uncoupling at subduction zones, *Tectonophysics*, *99*, 99–117.

Savage, J. C. (1983), A dislocation model of strain accumulation and release at a subduction zone, *J. Geophys. Res.*, *88*(B6), 4984–4996.

Sladen, A., H. Tavera, M. Simons, J. P. Avouac, A. O. Konca, H. Perfettini, L. Audin, E. J. Fielding, F. Ortega, and R. Cavagnoud (2010), Source model of the 2007 M_w 8.0 Pisco, Peru earthquake: Implications for seismogenic behavior of subduction megathrusts, *J. Geophys. Res.*, *115*, B02405, doi:10.1029/2009JB006429.

Sparkes, R., F. Tilmann, N. Hovius, and J. Hillier (2010), Subducted seafloor relief stops rupture in South American great earthquakes: Implications for rupture behavior in the 2010 Maule, Chile earthquake, *Earth Planet. Sci. Lett.*, *298*, 89–94.

Tassara, A., H. J. Gotze, S. Schmidt, and R. Hackney (2006), Three-dimensional density model of the Nazca plate and the Andean continental margin, *J. Geophys. Res.*, *111*, B09404, doi:10.1029/2005JB003976.

Tichelaar, B. W., and L. J. Ruff (1991), Seismic coupling along the Chilean subduction zone, *J. Geophys. Res.*, *96*(B7), 11,997–12,022.

Vigny, C., A. Rudloff, J. C. Ruegg, R. Madariaga, J. Campos, and M. Alvarez (2009), Upper plate deformation measured by GPS in the Coquimbo Gap, Chile, *Phys. Earth Planet. Inter.*, *175*(1–2), 86–95.

Vigny, C., et al. (2011), The 2010 (M_w 8.8) earthquake of central Chile monitored by GPS, *Science*, *332*(6036), 1417–1421, doi:10.1126/science.1204132.

Wang, K., and S. Bilek (2011), Do subducting seamounts generate or stop large earthquakes?, *Geology*, *39*(9), 819–822.

Wang, K., Y. Hu, M. Bevis, E. Kendrick, R. Smalley Jr, R. B. Vargas, and E. Lauría (2007), Crustal motion in the zone of the 1960 Chile earthquake: Detangling earthquake-cycle deformation and forearc-sliver translation, *Geochem. Geophys. Geosyst.*, *8*, Q10010, doi:10.1029/2007GC001721.

M. Métois and C. Vigny, Equipe de Géophysique, Laboratoire de Géologie, UMR 8538, Ecole Normale Supérieure, 24 rue Lhomond, F-75005 Paris, France. (metois@geologie.ens.fr)

A. Socquet, Institut des Sciences de la Terre, Université de Grenoble 1, CNRS, F-38041 Grenoble, France.